

## PAPER



Cite this: *Phys. Chem. Chem. Phys.*,  
2022, 24, 25663

# Kinetic and dynamic studies of the $\text{NH}_2^+ + \text{H}_2$ reaction on a high-level *ab initio* potential energy surface

Yongfa Zhu, \*<sup>a</sup> Rui Li<sup>a</sup> and Hongwei Song <sup>b</sup>

Gas-phase ion–molecule reactions have attracted considerable attention due to their importance in the fields of interstellar chemistry, plasma chemistry, and combustion chemistry. The reaction of an amino radical cation with a hydrogen molecule is one of the crucial steps in the gas-phase formation of ammonia in the interstellar medium (ISM). The dynamics and kinetics of the  $\text{NH}_2^+ + \text{H}_2$  reaction are studied using the quasi-classical trajectory approach on a newly constructed *ab initio* potential energy surface (PES) for the ground electronic state. The PES is fitted by the fundamental invariant-neural network method, resulting in a total root mean square error (RMSE) of  $0.061 \text{ kcal mol}^{-1}$ . Dynamics calculations show that, on one hand, the vibrational excitation of  $\text{H}_2$  largely promotes the reaction. On the other hand, the fundamental excitation of each vibrational mode of  $\text{NH}_2^+$  inhibits the reaction at low collision energies which has a negligible effect at high collision energies except for the symmetric stretching mode. The relatively higher efficacy of the symmetric stretching mode than that of the asymmetric stretching mode can be rationalized by the underlying reaction mechanisms. In addition, the calculated rate coefficients of the reaction agree reasonably well with the available experimental results.

Received 22nd August 2022,  
Accepted 4th October 2022

DOI: 10.1039/d2cp03859e

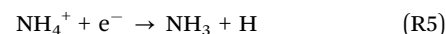
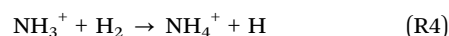
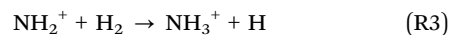
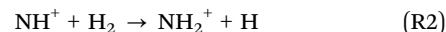
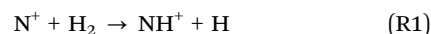
rsc.li/pccp

## 1. Introduction

Gas-phase ion–molecule reactions play a pivotal role in physical and chemical processes associated with interstellar chemistry, plasma chemistry, liquid solutions and combustion. Despite the fact that tremendous progress has been made both theoretically and experimentally over the past decades, our understanding of their reaction kinetics and dynamics is still not complete.<sup>1–15</sup> Since there exist strong long-range interactions of charged species with neutral atoms or molecules, this kind of reaction is usually expected to have a large scattering cross section for inelastic or reactive processes.<sup>16–24</sup>

Nitrogen hydrides are thought to be the precursors of nitrogen chemical networks owing to the dominance of hydrogen and nitrogen in the Universe. The chemical network of nitrogen in the interstellar medium (ISM) is, however, unclear due to the difficulty in observing key molecules from the ground.<sup>25–27</sup> Since its discovery as the first polyatomic molecule in interstellar space,<sup>28</sup>  $\text{NH}_3$  has been widely used as a temperature and

structural probe of dense cloud cores in star-forming regions or as a tracer of shocks along outflows emitted by young stars.<sup>29–31</sup> Both experimental and theoretical studies on the mechanism of  $\text{NH}_3$  formation and destruction under interstellar conditions are essential to simulate the abundance of various molecules in the ISM. The most likely routes to form  $\text{NH}_3$  in the ISM were thought to be a chain of hydrogen abstraction reactions followed by the dissociative recombination of ionic nitrogen hydrides.<sup>32–34</sup> The chain is initiated by  $\text{N}^+$  and the neutral  $\text{NH}_3$  is consequently formed in the dissociative recombination of  $\text{NH}_4^+$  with an electron, as listed below:



To mimic the production of ammonia in the ISM, it is important to know the kinetics and dynamics of all the reactions in the chain, knowledge of which is useful to validate several astrochemical models.<sup>33–35</sup>

Reaction (R3) is of interest in this work, in which the neutral molecule  $\text{H}_2(^1\Sigma_g^+)$  reacts with the amino radical cation  $\text{NH}_2^+(^3\text{B}_1)$

<sup>a</sup> School of Chemistry and Chemical Engineering, Hubei Polytechnic University, Huangshi 435003, China. E-mail: zhu yf@wipm.ac.cn

<sup>b</sup> State Key Laboratory of Magnetic Resonance and Atomic and Molecular Physics, Wuhan Institute of Physics and Mathematics, Innovation Academy for Precision Measurement Science and Technology, Chinese Academy of Sciences, Wuhan 430071, China

to yield  $\text{NH}_3^+ (^2\text{A}_2'')$  and  $\text{H}(^2\text{S})$  through a hydrogen abstraction. Early experimental attention has been paid to studying its kinetics at temperatures from 15 up to 300 K.<sup>36–40</sup> Fehsenfeld *et al.* measured the rate coefficients of the  $\text{NH}_2^+ + \text{H}_2 \rightarrow \text{NH}_3^+ + \text{H}$  reaction at 300 K in a flowing afterglow (FA) system to be  $1.0 \times 10^{-9} \text{ cm}^3 \text{ molecule}^{-1} \text{ s}^{-1}$ .<sup>36</sup> Using an ion cyclotron resonance (ICR) technique, Kim *et al.* obtained the rate coefficients of the  $\text{NH}_2^+ + \text{H}_2 \rightarrow \text{NH}_3^+ + \text{H}$  reaction to be about  $(1.2 \pm 0.2) \times 10^{-10} \text{ cm}^3 \text{ molecule}^{-1} \text{ s}^{-1}$  at 300 K.<sup>37</sup> The rate coefficient was determined to be  $2.7 \times 10^{-10} \text{ cm}^3 \text{ molecule}^{-1} \text{ s}^{-1}$  at 300 K by Adams *et al.* using a selected ion flow tube (SIFT) apparatus.<sup>38</sup> By applying an ion trap instrument, Gerlich measured the rate coefficient of the reaction to be  $2.7 \times 10^{-10} \text{ cm}^3$  at 15 K.<sup>39</sup> More recently, Rednyk *et al.* experimentally investigated the low-temperature reaction dynamics of  $\text{NH}_2^+ + \text{H}_2 \rightarrow \text{NH}_3^+ + \text{H}$  in a variable-temperature 22-pole radio frequency ion trap. They found that the measured rate coefficient monotonically decreases with the increasing temperature from  $6.0 \times 10^{-10} \text{ cm}^3 \text{ molecule}^{-1} \text{ s}^{-1}$  at 17 K to  $2.0 \times 10^{-10} \text{ cm}^3 \text{ molecule}^{-1} \text{ s}^{-1}$  at 300 K.<sup>40</sup>

Theoretically, Mohandas *et al.* reported the key features of the potential energy surface (PES) for the  $\text{NH}_2^+ + \text{H}_2 \rightarrow \text{NH}_3^+ + \text{H}$  reaction.<sup>41</sup> They concluded that this reaction is highly exoergic and proceeds by overcoming a tiny barrier (about  $0.364 \text{ kcal mol}^{-1}$  with zero-point energy corrections at the CCSD/aug-cc-pVTZ level). Experimental rate coefficients under interstellar conditions were well reproduced by introducing reaction path degeneracy (a factor of four) within the framework of transition-state theory (TST). In particular, the quantum mechanical tunneling was found to govern the reaction.<sup>41</sup> Another recent theoretical study<sup>42</sup> focused on the vibrational level calculations of the ammonium cation ( $\text{NH}_4^+$ ) based on a semiglobal PES at the CCSD(T)-F12a/cc-pCVTZ-F12 level, which, however, a dissociation limit corresponding to  $\text{NH}_4^+$  is  $\text{NH}_3 + \text{H}^+$  channel. Furthermore, *ab initio* calculations with frozen-core (FC) and all-electron (AE) treatments also show that the core electron correlation has a noticeable effect on the  $\text{NH}_4^+$  system.<sup>41,42</sup>

An accurate potential energy surface is the cornerstone of dynamics studies, which carries precise information about the underlying species and facilitates the analysis of all structural isomers, spectroscopy, and chemical reaction dynamics. In this work, a full-dimensional, globally accurate PES for the  $\text{NH}_2^+ + \text{H}_2$  reaction is developed by fitting 65 721 *ab initio* points calculated at the level of AE-UCCSD(T)-F12a/aug-cc-pVTZ<sup>43,44</sup> and using the fundamental invariant-neural network (FI-NN) method.<sup>45,46</sup> The dynamics and kinetics of the reaction are then investigated on the newly constructed PES using the quasi-classical trajectory (QCT) method.

## II. Potential energy surface

The accuracy of a PES is mainly determined by the level of *ab initio* methods and basis sets, sampling configurations in dynamically relevant regions and the fitting method.<sup>23,47–50</sup> Next, we briefly introduce how to construct the PES in this work.

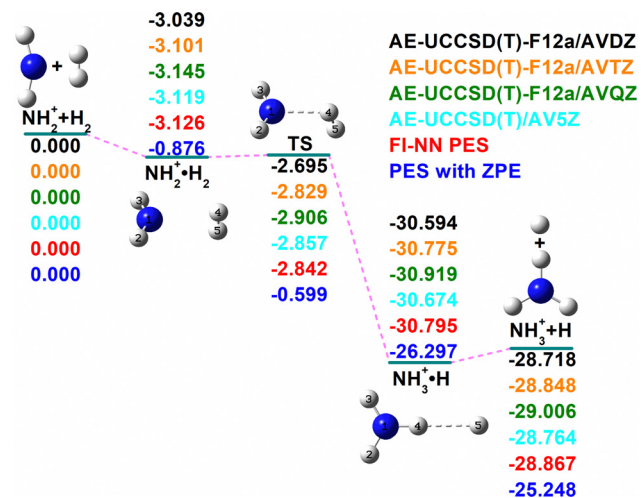


Fig. 1 Schematic diagram of the reaction path for the  $\text{NH}_2^+ + \text{H}_2$  reaction. All energies are in  $\text{kcal mol}^{-1}$  and relative to the reactant asymptote at various levels including AE-UCCSD(T)-F12a/AVDZ, AE-UCCSD(T)-F12a/AVTZ, AE-UCCSD(T)-F12a/AVQZ, AE-UCCSD(T)/AV5Z, FI-NN PES and the zero-point energy corrected values.

The performance of different *ab initio* methods and basis sets, including MP2/aug-cc-pVnZ, CCSD/aug-cc-pVnZ, CCSD(T)/aug-cc-pVnZ, and CCSD(T)/CBS ( $n = 2, 3, 4, 5$  and  $6$ ), has been assessed by Mohandas *et al.*<sup>41</sup> They concluded that there was no significant multireference character in the wave function and thus a single determinant treatment is suffice. In this work, the geometries of stationary points along the minimum energy path (MEP) are first optimized at the level of AE-UCCSD(T)-F12a/aug-cc-pVDZ, AE-UCCSD(T)-F12a/aug-cc-pVTZ, AE-UCCSD(T)-F12a/aug-cc-pVQZ, and AE-UCCSD(T)/aug-cc-pV5Z. The explicit treatment of the electron–electron interaction (F12) demonstrates much faster convergence to the complete basis set limit.<sup>43,44</sup> The T1 diagnostic (less than 0.05) is also carefully checked, which has been suggested as an indicator of the quality of a CCSD wave function.<sup>51</sup> Then, the energies and harmonic frequencies of these geometries are also computed at the same levels for comparison (see Fig. 1 and Tables 1–3). Table 1 summarizes the zero-point energy (ZPE) corrected energies of the stationary points at different levels. Clearly, the results are sensitive to the employed *ab initio*

Table 1 ZPE corrected energies (in  $\text{kcal mol}^{-1}$ ) of the stationary points at various levels

	$\text{NH}_2^+ + \text{H}_2$	$\text{NH}_2^+\cdot\text{H}_2$	TS	$\text{NH}_3^+\cdot\text{H}$	$\text{NH}_3^+ + \text{H}$
FI-NN PES <sup>a</sup>	0.000	−0.876	−0.599	−26.297	−25.248
<i>Ab initio</i> <sup>b</sup>	0.000	−0.843	−0.428	−26.022	−25.063
<i>Ab initio</i> <sup>c</sup>	0.000	−0.857	−0.580	−26.252	−25.230
<i>Ab initio</i> <sup>d</sup>	0.000	−0.876	−0.663	−26.393	−25.385
<i>Ab initio</i> <sup>e</sup>	0.000	−0.819	−0.622	−26.153	−25.148
Mohandas <sup>f</sup>	0.000	−0.709	0.734	−29.258	−28.373
Mohandas <sup>g</sup>	0.000	−0.688	0.364	−24.088	−23.127
ATcT <sup>h</sup>	0.000				−25.397

<sup>a</sup> This work, FI-NN PES. <sup>b</sup> This work, AE-UCCSD(T)-F12a/AVDZ. <sup>c</sup> This work, AE-UCCSD(T)-F12a/AVTZ. <sup>d</sup> This work, AE-UCCSD(T)-F12a/AVQZ. <sup>e</sup> This work, AE-UCCSD(T)/AV5Z. <sup>f</sup> Ref. 41, FC-MP2/AVTZ. <sup>g</sup> Ref. 41, FC-CCSD/AVTZ. <sup>h</sup> Ref. 52, ATcT.

levels and the largest discrepancy exists for the activation energy. Using the same basis set of aug-cc-pVTZ, we obtain a negative activation barrier ( $-0.580 \text{ kcal mol}^{-1}$  at the level of UCCSD(T)-F12a) after including the zero-point energy corrections, while a positive barrier was reported by Mohandas *et al.* at the CCSD (or MP2) level of theory.<sup>41</sup> However, this submerged barrier is indeed confirmed by highly expensive quantum chemical calculations such as AE-UCCSD(T)-F12a/AVQZ and AE-UCCSD(T)/AV5Z. The ZPE corrected reaction energy of the separated products is  $-25.230 \text{ kcal mol}^{-1}$  at the AE-UCCSD(T)-F12a/AVTZ level and  $-25.285 \text{ kcal mol}^{-1}$  at the AE-UCCSD(T)-F12a/AVQZ level, close to the AE-UCCSD(T)/AV5Z value of  $-25.148 \text{ kcal mol}^{-1}$  and the ATcT value of  $-25.397 \text{ kcal mol}^{-1}$ .<sup>52</sup> Moreover, the classical energy of the saddle point is  $-2.829 \text{ kcal mol}^{-1}$  close to the AE-UCCSD(T)/AV5Z value of  $-2.857 \text{ kcal mol}^{-1}$ . To balance the accuracy and computational cost, AE-UCCSD(T)-F12a/AVTZ is finally employed in the following single point energy calculations. All the *ab initio* calculations are carried out employing the Molpro 2012 software.<sup>53</sup>

To sample data points in the relevant configuration space, 2-dimensional (2D) denser grids along the MEP and its tangential direction are first generated with the energy spanning roughly  $90 \text{ kcal mol}^{-1}$  from  $-30$  to  $60 \text{ kcal mol}^{-1}$  with respect to the reactant asymptote. For the 2D grid points, the reactants are initiated from a separation of  $30 \text{ \AA}$  and the products are ended with a separation of  $25 \text{ \AA}$ . Then, starting with these initial grids, atom centered density matrix propagation (ADMP) molecular dynamics is carried out by implementing Gaussian 09, Revision B.01<sup>54</sup> at the level of B3LYP/6-311G\*. The first batch of data points

is selected from these ADMP trajectories to generate a raw PES. Based on this raw PES, batches of quasi-classical trajectories are run with specific vibrational/rotational/translational temperatures to explore all dynamically relevant regions. The points from these trajectories whose geometries are close to the existing data set are eliminated by using the Euclidean distance

$$\chi = \sqrt{\sum_{i=1}^{10} |\vec{r}_i - \vec{r}_j|^2} < 0.1 - 0.4 \text{ \AA}, \text{ which is defined in terms of}$$

the internuclear distance between two points  $\{\vec{r}_i\}$  and  $\{\vec{r}_j\}$ , respectively. All the permutationally equivalent points among four hydrogen atoms ( $4! = 24$ ) are considered in such a screening. The remaining data points which have large energy uncertainties on different PESs are selected and added to the previous data set to patch up the non-physical region of the raw PES. The procedure was repeated dozens of times to guarantee that all the key properties of PESs, including geometries, frequencies, and energies of the stationary points, regions around the MEPs and the energy conservation during QCT propagations are satisfied. The PES is considered to be converged when the calculated cross sections and rate coefficients do not change with an increase in the number of data points, like the GROW procedure.<sup>55</sup> Finally, a total of 65 721 points calculated at the level of AE-UCCSD(T)-F12a/AVTZ are retained in the data set.

The fundamental invariant-neural network<sup>45,46</sup> method is utilized in the fitting and the resulting PES is denoted as the FI-NN PES hereafter. For the FI-NN approach, the permutation symmetry of identical atoms in the system is enforced by

**Table 2** Geometries (bond length in angstrom and angle in degree) of the stationary points for the  $\text{NH}_2^+ + \text{H}_2 \rightarrow \text{NH}_3^+ + \text{H}$  reaction. The corresponding atom labels are given in Fig. 1

Species	Method	$R_{\text{N}_1\text{H}_2}$	$R_{\text{N}_1\text{H}_3}$	$R_{\text{N}_1\text{H}_4}$	$R_{\text{H}_4\text{H}_5}$	$\theta_{\text{H}_2\text{N}_1\text{H}_3}$	$\theta_{\text{H}_2\text{N}_1\text{H}_4}$	$\theta_{\text{N}_1\text{H}_4\text{H}_5}$	$\phi_{\text{H}_4\text{N}_1\text{H}_2\text{H}_3}$	$\phi_{\text{H}_3\text{H}_4\text{N}_1\text{H}_2}$
$\text{NH}_2^+ + \text{H}_2$	FI-NN PES <sup>a</sup>	1.031	1.031		0.742	152.40				
	<i>Ab initio</i> <sup>b</sup>	1.033	1.033		0.746	152.34				
	<i>Ab initio</i> <sup>c</sup>	1.031	1.031		0.742	152.46				
	<i>Ab initio</i> <sup>d</sup>	1.031	1.031		0.741	152.36				
	<i>Ab initio</i> <sup>e</sup>	1.031	1.031		0.742	152.19				
$\text{NH}_2^+ \cdot \text{H}_2$	FI-NN PES <sup>a</sup>	1.029	1.029	2.176	0.759	142.55	108.43	79.96	169.41	93.38
	<i>Ab initio</i> <sup>b</sup>	1.030	1.030	2.215	0.761	143.68	107.88	80.11	169.64	93.25
	<i>Ab initio</i> <sup>c</sup>	1.028	1.028	2.179	0.759	142.73	108.35	80.02	169.44	93.37
	<i>Ab initio</i> <sup>d</sup>	1.028	1.028	2.162	0.759	142.21	108.60	79.90	169.35	93.42
	<i>Ab initio</i> <sup>e</sup>	1.028	1.028	2.170	0.759	142.17	108.59	79.92	169.37	93.41
TS	FI-NN PES <sup>a</sup>	1.027	1.027	1.822	0.775	135.96	111.73	106.28	170.21	93.66
	<i>Ab initio</i> <sup>b</sup>	1.029	1.029	1.823	0.778	136.20	111.69	107.90	171.60	93.13
	<i>Ab initio</i> <sup>c</sup>	1.027	1.027	1.827	0.774	136.08	111.72	106.17	171.18	93.27
	<i>Ab initio</i> <sup>d</sup>	1.027	1.027	1.830	0.774	136.04	111.74	105.23	171.05	93.32
	<i>Ab initio</i> <sup>e</sup>	1.027	1.027	1.827	0.774	136.00	111.76	106.13	171.17	93.29
	Mohandas <sup>f</sup>	1.027	1.027	1.773	0.777	135.87	111.91	118.06	172.77	92.71
	Mohandas <sup>g</sup>	1.023	1.023	1.780	0.776	136.02	111.83	116.53	172.61	92.76
$\text{NH}_3^+ \cdot \text{H}$	FI-NN PES <sup>a</sup>	1.021	1.021	1.028	1.912	119.73	120.13	180.00	180.00	180.00
	<i>Ab initio</i> <sup>b</sup>	1.022	1.022	1.029	1.909	119.68	120.16	179.85	180.00	180.00
	<i>Ab initio</i> <sup>c</sup>	1.021	1.021	1.028	1.906	119.68	120.16	180.00	180.00	180.00
	<i>Ab initio</i> <sup>d</sup>	1.021	1.021	1.028	1.907	119.68	120.16	179.49	180.00	180.00
	<i>Ab initio</i> <sup>e</sup>	1.021	1.021	1.028	1.909	119.70	120.16	179.19	180.00	180.00
$\text{NH}_3^+ + \text{H}$	FI-NN PES <sup>a</sup>	1.021	1.021	1.021		120.00	120.00		180.00	
	<i>Ab initio</i> <sup>b</sup>	1.023	1.022	1.022		120.00	120.00		180.00	
	<i>Ab initio</i> <sup>c</sup>	1.021	1.021	1.021		120.00	120.00		180.00	
	<i>Ab initio</i> <sup>d</sup>	1.021	1.021	1.021		120.00	120.00		180.00	
	<i>Ab initio</i> <sup>e</sup>	1.021	1.021	1.021		120.00	120.00		180.00	

<sup>a</sup> This work, FI-NN PES. <sup>b</sup> This work, AE-UCCSD(T)-F12a/AVDZ. <sup>c</sup> This work, AE-UCCSD(T)-F12a/AVTZ. <sup>d</sup> This work, AE-UCCSD(T)-F12a/AVQZ.

<sup>e</sup> This work, AE-UCCSD(T)/AV5Z. <sup>f</sup> Ref. 41, FC-CCSD/AVTZ. <sup>g</sup> Ref. 41, AE-CCSD/AVTZ.

**Table 3** Energies (in kcal mol<sup>-1</sup>) and harmonic frequencies (in cm<sup>-1</sup>) of the stationary points for the NH<sub>2</sub><sup>+</sup> + H<sub>2</sub> → NH<sub>3</sub><sup>+</sup> + H reaction

Species	Method	Energy	Frequency (cm <sup>-1</sup> )								
			1	2	3	4	5	6	7	8	9
NH <sub>2</sub> <sup>+</sup> + H <sub>2</sub>	FI-NN PES <sup>a</sup>	0.000	4393	3526	3264	731					
	<i>Ab initio</i> <sup>b</sup>	0.000	4385	3504	3248	744					
	<i>Ab initio</i> <sup>c</sup>	0.000	4401	3511	3256	737					
	<i>Ab initio</i> <sup>d</sup>	0.000	4404	3515	3259	741					
	<i>Ab initio</i> <sup>e</sup>	0.000	4403	3515	3259	746					
	Mohandas <sup>f</sup>	0.000	4401	3524	3270	751					
NH <sub>2</sub> <sup>+</sup> ·H <sub>2</sub>	Mohandas <sup>g</sup>		4401	3539	3311	751					
	FI-NN PES <sup>a</sup>	-3.126	4118	3541	3303	957	451	395	308	233	183
	<i>Ab initio</i> <sup>b</sup>	-3.039	4143	3534	3286	940	424	393	292	233	172
	<i>Ab initio</i> <sup>c</sup>	-3.101	4128	3540	3296	956	441	387	310	241	176
	<i>Ab initio</i> <sup>d</sup>	-3.145	4118	3546	3301	969	453	381	318	246	174
	<i>Ab initio</i> <sup>e</sup>	-3.119	4118	3546	3302	972	451	391	316	246	191
TS	Mohandas <sup>f</sup>	-2.620	4227	3547	3297	873	420	327	223	222	160
	Mohandas <sup>g</sup>		4216	3565	3338	885	414	337	236	221	161
	FI-NN PES <sup>a</sup>	-2.842	3837	3551	3320	1106	586	471	429	184	501 <i>i</i>
	<i>Ab initio</i> <sup>b</sup>	-2.695	3835	3540	3311	1109	584	478	424	186	518 <i>i</i>
	<i>Ab initio</i> <sup>c</sup>	-2.829	3848	3545	3317	1104	583	469	432	180	491 <i>i</i>
	<i>Ab initio</i> <sup>d</sup>	-2.906	3856	3550	3320	1106	584	467	433	172	484 <i>i</i>
NH <sub>3</sub> <sup>+</sup> ·H	<i>Ab initio</i> <sup>e</sup>	-2.857	3851	3549	3320	1108	583	468	433	175	487 <i>i</i>
	Mohandas <sup>f</sup>	-1.771	3767	3557	3332	1115	583	499	418	167	602 <i>i</i>
	Mohandas <sup>g</sup>		3783	3577	3371	1123	587	503	414	182	584 <i>i</i>
	FI-NN PES <sup>a</sup>	-30.795	3554	3487	3301	1553	1539	883	329	251	164
	<i>Ab initio</i> <sup>b</sup>	-30.594	3553	3485	3298	1552	1546	891	319	264	171
	<i>Ab initio</i> <sup>c</sup>	-30.775	3557	3487	3300	1550	1544	881	324	256	170
NH <sub>3</sub> <sup>+</sup> + H	<i>Ab initio</i> <sup>d</sup>	-30.919	3561	3491	3304	1551	1545	883	325	257	168
	<i>Ab initio</i> <sup>e</sup>	-30.674	3561	3492	3304	1552	1546	882	324	257	168
	Mohandas <sup>f</sup>	-28.621	3569	3503	3324	1559	1553	870	320	247	171
	Mohandas <sup>g</sup>		3583	3518	3360	1577	1567	887	322	280	188
	FI-NN PES <sup>a</sup>	-28.867	3559	3559	3372	1546	1546	864			
	<i>Ab initio</i> <sup>b</sup>	-28.718	3550	3550	3366	1550	1550	872			
NH <sub>3</sub> <sup>+</sup> + H	<i>Ab initio</i> <sup>c</sup>	-28.848	3553	3553	3370	1548	1548	864			
	<i>Ab initio</i> <sup>d</sup>	-29.006	3558	3558	3373	1549	1549	865			
	<i>Ab initio</i> <sup>e</sup>	-28.764	3558	3558	3373	1550	1550	864			
	Mohandas <sup>f</sup>	-26.752	3565	3565	3385	1556	1556	852			
	Mohandas <sup>g</sup>		3582	3582	3421	1574	1574	870			

<sup>a</sup> This work, FI-NN PES. <sup>b</sup> This work, AE-UCCSD(T)-F12a/AVDZ. <sup>c</sup> This work, AE-UCCSD(T)-F12a/AVTZ. <sup>d</sup> This work, AE-UCCSD(T)-F12a/AVQZ. <sup>e</sup> This work, AE-UCCSD(T)/AV5Z. <sup>f</sup> Ref. 41, FC-CCSD/AVTZ. <sup>g</sup> Ref. 41, AE-CCSD/AVTZ.

introducing the fundamental invariant polynomials (FIs) into the NN as input,<sup>39,40</sup> which shares the same spirit as the permutation invariant polynomial neural network (PIP-NN) approach.<sup>56,57</sup> Theoretically, the NN fitting can approximate any function to any accuracy provided that enough data points are sampled in the relevant configuration space.<sup>58</sup> The Morse-like variables  $P_{ij} = \exp(-r_{ij}/\alpha)$  are used to construct the polynomials ( $\alpha$  is taken as 3.0 Å in this work), in which  $r_{ij}$  is the nuclear distance between the  $i$ th and the  $j$ th atoms.<sup>59</sup> For the system such as AB<sub>4</sub>, there exist 31 fundamental invariants with a maximum degree of 4. The architecture of NN is selected to be 31-30-30-1, yielding a total of 1921 parameters. The input layer of the NN contains 31 FIs, the two hidden layers consist of 30 and 30 neurons, and the output layer has 1 potential energy. In each NN fitting, the data are randomly divided into three groups, 90% of the points as the training set, 5% as the validating set and 5% as the testing sets. All fittings are implemented using the Levenberg–Marquardt algorithm.<sup>58,60</sup> The root mean square error (RMSE), defined as  $\text{RMSE} =$

$\sqrt{\sum_{i=1}^{N_{\text{data}}} (E_{\text{fit}} - E_{\text{ab initio}})^2 / N_{\text{data}}}$ , is employed to assess the quality of each fitting. Finally, the so-called ensemble approach is used to

minimize random errors.<sup>61</sup> The overall RMSE of the final PES is only 0.061 kcal mol<sup>-1</sup>, which is an average of four PESs with the training/validating/testing RMSEs of 0.074/0.092/0.095, 0.074/0.092/0.099, 0.074/0.092/0.125 and 0.074/0.090/0.085 kcal mol<sup>-1</sup>, respectively.

### III. Quasi-classical trajectory calculations

Standard QCT calculations are implemented on the newly developed FI-NN PES by the software VENUS 96.<sup>62</sup> The integral cross section (ICS) of the reaction is given by

$$\sigma_r(E_c) = \pi b_{\text{max}}^2 \frac{N_r}{N_{\text{tot}}}, \quad (1)$$

where  $N_r$  and  $N_{\text{tot}}$  are the numbers of reactive and total trajectories at a specified collision energy  $E_c$ . The maximum impact parameter  $b_{\text{max}}$  is determined by small batches of trajectories with trial values at each specified initial state. The impact parameter  $b$  is selected randomly from the distribution  $R^{1/2}b_{\text{max}}$ , in which  $R$  is a random number uniformly distributed from 0 to 1. The relative statistical error is measured by



$A = \sqrt{(N_{\text{tot}} - N_r)/N_{\text{tot}}N_r}$ . The zero-point energy (ZPE) leakage is the intrinsic defect in classical trajectory simulations, especially for low temperature and low energy. It should be noted that applying “ZPE constraints” sometimes can lead to unphysical results.<sup>23,63</sup> We did not present the dynamic and kinetic results with the ZPE constraints in this work.

The differential cross section (DCS) is obtained by

$$\frac{d\sigma_r}{d\Omega} = \frac{\sigma_r P_r(\theta)}{2\pi \sin(\theta)}, \quad (2)$$

where  $P_r(\theta)$  is the normalized probability. The scattering angle  $\theta$  is defined as

$$\theta = \cos^{-1} \left( \frac{\vec{v}_i \cdot \vec{v}_f}{|\vec{v}_i||\vec{v}_f|} \right), \quad (3)$$

in which  $\vec{v}_i = \vec{v}_{\text{NH}_2^+} - \vec{v}_{\text{H}_2}$  and  $\vec{v}_f = \vec{v}_{\text{NH}_3^+} - \vec{v}_{\text{H}}$  denote the relative velocity vector for the initial and final positions. Thus, trajectories with  $\theta = 0^\circ$  and  $\theta = 180^\circ$  correspond to the forward and backward scattering, respectively.  $P_r(\theta)$  in eqn (2) is obtained by

$$P_r(\theta) = \frac{\sum_{\theta-\Delta\theta}^{\theta+\Delta\theta} N_r(\theta)}{N_r}, \quad (4)$$

where  $\Delta\theta$  is taken as  $5.0^\circ$  in the calculations.

The thermal rate coefficients of R3 at temperatures of 15, 20, 25, 35, 45, 55, 75, 100, 200 and 300 K are calculated according to the following formula:

$$k(T) = \left( \frac{8k_B T}{\pi\mu} \right)^{1/2} \pi b_{\text{max}}^2 \frac{N_r}{N_{\text{tot}}},$$

where  $T$  is the temperature,  $\mu$  is the reduced mass between the reactants  $\text{NH}_2^+$  and  $\text{H}_2$ , and  $k_B$  is the Boltzmann constant. At each specific temperature  $T$ , the translational, vibrational, and rotational degrees of freedom of the two reactants are sampled according to the Boltzmann distribution. The thermal sampling assumes a symmetric top.

In dynamics calculations, trajectories are launched from a reactant separation of 25 Å and ended when the separation of products for reactive trajectories or reactants for nonreactive trajectories is larger than 20 Å. The time step is set as 0.05 fs, which conserves the total energy better than  $10^{-4}$  kcal mol<sup>-1</sup> during the propagation. For each initial state, 50 000–150 000 trajectories are run, guaranteeing that the relative statistical errors are all below 3%. The convergence of the dynamical properties based on these parameters involved in trajectory simulations is inspected and these values are also suitable for the thermal rate coefficient calculations.

## IV. Results and discussion

### A. Features of potential energy surfaces

Fig. 1 shows the schematic diagram of the reaction path for the hydrogen abstraction reaction  $\text{NH}_2^+ + \text{H}_2 \rightarrow \text{NH}_3^+ + \text{H}$ . The geometries of all stationary points are given in the figure, together with the corresponding *ab initio* energy at various

levels, the fitted energy, and the zero-point energy (ZPE) corrected energy. There exists a submerged barrier TS with  $C_s$  symmetry, whose energy is slightly lower than the reactant asymptote by 2.829 kcal mol<sup>-1</sup>. The transition state is flanked by two ion-dipole complexes ( $\text{NH}_2^+ \cdot \text{H}_2$  and  $\text{NH}_3^+ \cdot \text{H}$ ), whose energies are -3.101 and -30.775 kcal mol<sup>-1</sup> relative to the reactant asymptote. Along the MEP, a hydrogen in the  $\text{H}_2$  moiety of  $\text{NH}_2^+ \cdot \text{H}_2$  is transferred to the  $\text{NH}_2^+$  moiety by overcoming the transition state TS to form a product complex  $\text{NH}_3^+ \cdot \text{H}$  that then eventually dissociates to products  $\text{NH}_3^+ + \text{H}$ . The product energy is -28.848 kcal mol<sup>-1</sup>.

The optimized geometries of stationary points are given in Table 2. The FI-NN PES reproduces well the target AE-UCCSD(T)-F12a/AVTZ results. The difference between the fitted and *ab initio* values is less than 0.01 Å for each bond length and less than  $1^\circ$  for each angle. The energies and harmonic frequencies of the stationary points are listed in Table 3. One can see that the imaginary frequency for the saddle point at the AE-UCCSD(T)-F12a/AVTZ level is very close to that at the AE-UCCSD(T)/AV5Z level (-491 vs. -487), but differs noticeably from the values of Mohandas *et al.* at the CCSD/AVTZ level which are believed to be caused by the accuracy of the *ab initio* method. Regardless of energies and harmonic frequencies, the fitting values are in good agreement with the *ab initio* calculations. The deviations of energies and harmonic frequencies are within 0.02 kcal mol<sup>-1</sup> and 15 cm<sup>-1</sup>, respectively. These discrepancies are expected to have a negligible effect on the reaction dynamics.

The fitting errors of the sampled data points are shown in Fig. 2 as a function of energy. The fitting error is defined as the deviation of the fitted energy from the corresponding *ab initio* energy. They are dominantly distributed within the range of  $\pm 0.4$  kcal mol<sup>-1</sup> over the whole energy range studied. Very few points are scattered within  $[-0.4, -1.0]$  and  $[0.4, 1.0]$ . This distribution indicates that the FI-NN method has good flexibility to represent the PES. Fig. 3 depicts the contours of the PES as a function of the bond lengths of the breaking bond

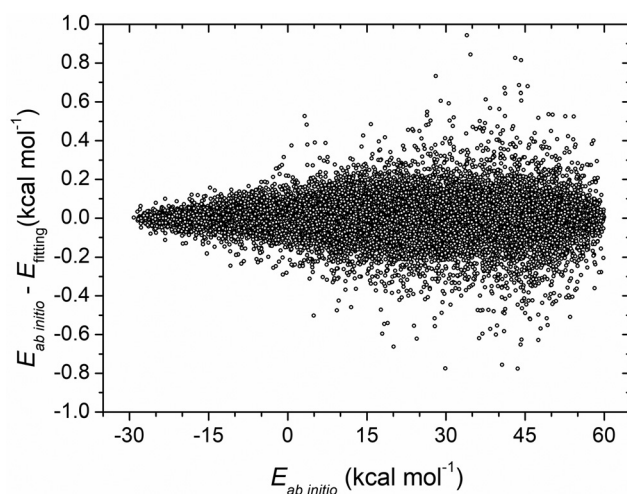


Fig. 2 Distribution of fitting errors ( $E_{\text{ab initio}} - E_{\text{fitting}}$ ) as a function of energy.

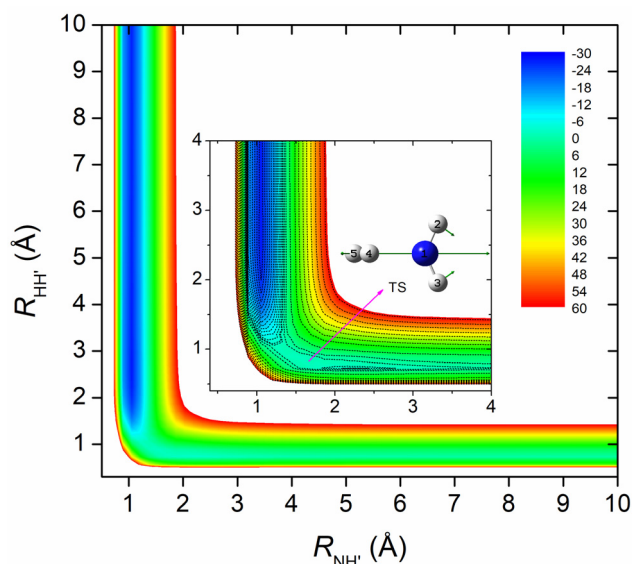


Fig. 3 Contour plot of the potential energy (in kcal mol<sup>-1</sup>) as a function of bond lengths of the breaking HH' and the forming NH' with the other coordinates fixed at the transition state.

$R_{\text{H}'\text{H}}$  ( $\text{H}_2\text{NH}'\text{-H}$ ) and the forming bond  $R_{\text{NH}'}$  ( $\text{H}_2\text{N-H}'\text{H}$ ). All the other internal coordinates are fixed at the transition state geometry. The energy is taken from  $-30$  to  $60$  kcal mol<sup>-1</sup> with an interval of  $6$  kcal mol<sup>-1</sup>. Obviously, the fitted PES is globally smooth and there does not exist any artificial pits. By plotting the contours along different dimensions, the existence of any other artificial pits is excluded. The pre- and post-reaction wells and the submerged barrier are clearly displayed in the inset.

Fig. 4 displays the MEP of the reaction determined by the software Polyrate 9.7 in mass-weighted Cartesian coordinates with a step size of  $5.0 \times 10^{-5}$  amu<sup>1/2</sup> Å.<sup>64</sup> The reaction coordinate  $s$  is defined as the signed distance from the saddle point ( $s = 0$ ), with  $s > 0$  referring to the product side and  $s < 0$  representing the

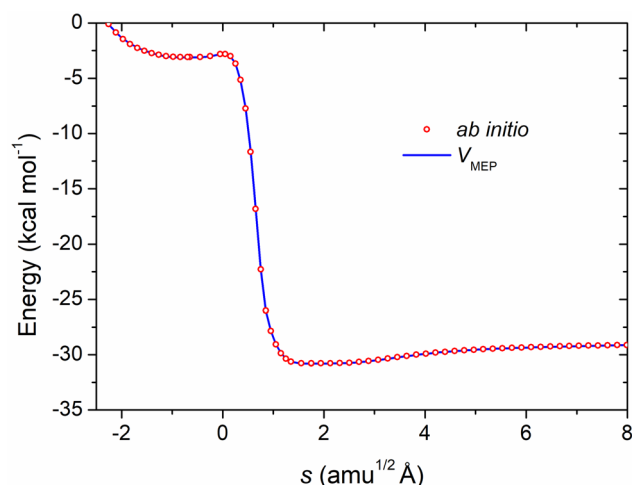


Fig. 4 Comparison of the fitted (solid line) and *ab initio* (circle) potential energies along the MEP for the  $\text{NH}_2^+ + \text{H}_2 \rightarrow \text{NH}_3^+ + \text{H}$  reaction. The *ab initio* energies are calculated at the level of AE-UCCSD(T)-F12a/AVTZ.

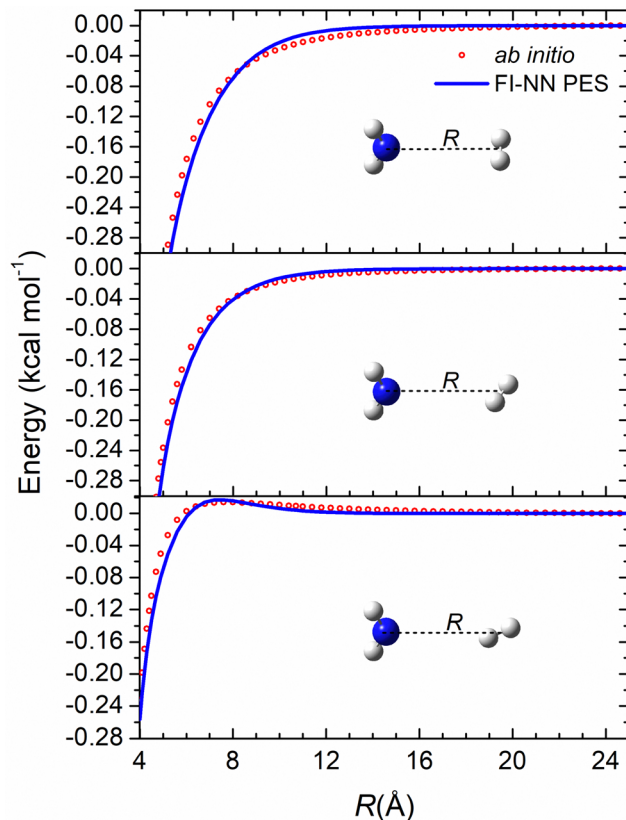


Fig. 5 Comparison of the *ab initio* and fitted potential energies along different attacking angles in the reactant asymptote.  $R$  is defined as the distance between the centers of mass of the two reactants.  $\text{NH}_2^+$  and  $\text{H}_2$  are fixed at their equilibrium geometries.

reactant side. The MEP starts from the saddle point geometry and goes downhill to the pre- and post-reaction wells. To further assess the accuracy of the fitted PES, single point energy calculations along the MEP are also performed at the level of AE-UCCSD(T)-F12a/AVTZ. Clearly, the MEP on the PES and the *ab initio* calculation are nearly superposed, suggesting a good description of the reaction path for the PES.

For the ion-molecule reaction, the long-range interaction usually plays a significant role in chemical reaction dynamics, especially at low temperatures.<sup>9</sup> Thus, to describe the long-range interaction reasonably, the sampled configuration space must cover the long-range interaction region. Fig. 5 compares the *ab initio* energies with the fitted potential energies along different attacking angles. As shown in Fig. 5, the deviations between the FI-NN PES and the *ab initio* calculations in long-range regions (larger than  $8$  Å) are less than  $0.02$  kcal mol<sup>-1</sup> even if the distances reach  $25$  Å, while the largest difference in short-range regions is only about  $0.03$  kcal mol<sup>-1</sup>. Overall, both long- and short-range regions are well reproduced by the current PES with high accuracy.

## B. Dynamics

Fig. 6 depicts the calculated ICSs as a function of collision energy ( $E_c$ ) from the ground and fundamental states of  $\text{H}_2$  and  $\text{NH}_2^+$ .

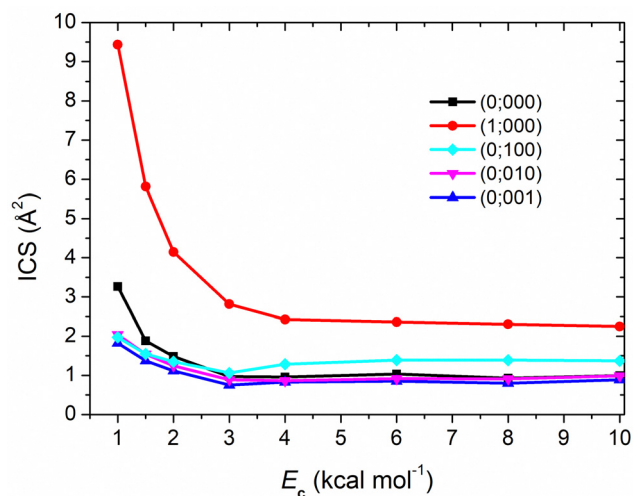


Fig. 6 Integral cross sections (ICSs) of the  $\text{NH}_2^+ + \text{H}_2$  reaction from the ground and fundamental states of reactants  $\text{NH}_2^+$  and  $\text{H}_2$  as a function of collision energy  $E_c$ .

The initial vibrational states of reactants are labelled as  $(\nu_{\text{H}_2}; \nu_1, \nu_2, \nu_{13})$ , in which  $\nu_{\text{H}_2}$  denotes the vibrational excitation in  $\text{H}_2$ , and  $\nu_1, \nu_2$ , and  $\nu_3$  refer to excitations in the symmetric stretching mode, the bending mode, and the antisymmetric stretching mode of  $\text{NH}_2^+$ , respectively. The ICS decreases monotonically and then becomes nearly flat as the collision energy increases, which satisfies the character of barrierless reactions. Excitation of the  $\text{H}_2$  vibrational mode has the highest efficacy in promoting the reaction over the collision energy range studied. This promotional effect on the reactivity is easily understood considering that the vibrational motion of  $\text{H}_2$  is actually along the reaction coordinate, which is supported by the vibrational normal mode vector of the imaginary frequency of the transition state in Fig. 3. However, when the symmetric stretching mode (100) is excited, the ICS first descends rapidly with the increase of the collision energy, rises monotonically from 3.0 to 4.0  $\text{kcal mol}^{-1}$ , and then becomes nearly unchanged. Therefore, the reaction has a character of the barrierless reaction in the energy range below around 3.0  $\text{kcal mol}^{-1}$ , in which the ICS decreases as the collision energy increases. As the collision energy increases to above 3.0  $\text{kcal mol}^{-1}$ , the reaction behaves like an activated reaction, in which the ICS increases with the collision energy. By analyzing the reactive trajectories, it is found that the initial orientation of reactants favors the collider to form a transition state structure and thus the transition state is thought to be a bottleneck of the reaction although the classical barrier is submerged. These dynamical features are also found in other barrierless reactions, such as  $\text{OH} + \text{H}_2\text{S}$  and  $\text{OH} + \text{HO}_2$  reactions.<sup>65,66</sup>

In addition, one can see that exciting the symmetric stretching mode ( $\nu_1$ ) is always more efficient than exciting the asymmetric stretching mode ( $\nu_3$ ) of  $\text{NH}_2^+$ . Considering that the *ab initio* frequency of 3511  $\text{cm}^{-1}$  for fundamental excitation of  $\nu_1$  is only 255  $\text{cm}^{-1}$  higher than that of 3256  $\text{cm}^{-1}$  for  $\nu_3$  (see Table 3), the larger efficiency of the  $\nu_1$  stretching mode than the  $\nu_3$  stretching mode is intriguing. At high collision energies above 3.0  $\text{kcal mol}^{-1}$ , excitation of each vibrational mode of  $\text{NH}_2^+$  has negligible effect on

the reaction except for the symmetric stretching mode ( $\nu_1$ ), indicating that the bending mode ( $\nu_2$ ) and the antisymmetric stretching mode ( $\nu_3$ ) of  $\text{NH}_2^+$  have little coupling with the reaction coordinate and thus their vibrational energy cannot flow into the reaction coordinate effectively. This novel mode-specific behavior can be rationalized by the fact that the bond length of  $\text{NH}$  varies along the MEP. As shown in Table 2, two equal  $\text{NH}$  bond lengths are 1.031, 1.028, 1.027, 1.021, and 1.021 Å for  $\text{NH}_2^+$ ,  $\text{NH}_2^+ \cdot \text{H}_2$ , TS,  $\text{NH}_3^+ \cdot \text{H}$ , and  $\text{NH}_3^+$ , respectively. The synchronous decrease of  $\text{NH}$  bond length suggests that the excitation of the symmetric stretching mode will eventually promote the occurrence of the reaction along the MEP.

Furthermore, the vibrational excitation of each vibrational mode of  $\text{NH}_2^+$  inhibits the reaction at collision energies below 3.0  $\text{kcal mol}^{-1}$ . Due to the barrierless nature of the title reaction, the chemical reactivity at low collision energy is largely determined by the long-range electrostatic interactions in the entrance channel, including the charge-quadrupole and charge-induced dipole.<sup>41</sup> These interactions are proportional to  $r^{-3}$  and  $r^{-4}$ , respectively, where  $r$  is the distance between the center-of-charges of reactants. This suppression of the vibrational excitation on the reactivity may be attributed to the fact that the vibrational excitation of  $\text{NH}_2^+$  enlarges  $r$  and thus reduces the long-range interaction, especially for the bending mode, which resembles the previous study on the ion-molecule reactions  $\text{H}_2\text{O}^+ + \text{H}_2$ ,<sup>20</sup> both with submerged barriers.

To unveil the microscopic reaction mechanism, Fig. 7(a) shows the differential cross sections (DCSSs) of the  $\text{NH}_2^+ + \text{H}_2 \rightarrow \text{NH}_3^+ + \text{H}$  reaction from the reactant ground state with the collision energies fixed at 1.0, 1.5, 2.0, 3.0, 4.0, 6.0, 8.0 and 10.0  $\text{kcal mol}^{-1}$ , respectively. At low collision energies, the DCS shows a nearly forward-backward symmetric distribution, originating from the long-lived reaction intermediate formed in the reaction. For most of the reactive trajectories the colliders are firstly trapped in the reactant well with the  $\text{H}_2$  moiety rotating around the  $\text{NH}_2^+$  moiety and then evolve into the product well with one of the dissociated H rotating around the  $\text{NH}_3^+$  moiety, indicating that the reaction is dominated by the indirect mechanism. As the collision energy increases, the DCSs become almost isotropically distributed and the reaction somewhat favors backward scattering.

To further clarify the disparate efficiencies of the two stretching modes, Fig. 7(b) compares the DCSs for the fundamental excitation of symmetric ( $\nu_1$ ) and asymmetric stretching modes ( $\nu_3$ ). At low collision energies, the DCSs for the fundamental excitation of  $\nu_1$  are somewhat larger than those of the  $\nu_3$  mode, because the  $\nu_1$  mode of  $\text{NH}_2^+$  is expected to favor the formation of the ion-dipole complexes along the MEP that enhances the reaction by the indirect mechanism. With the increase of collision energy, the DCSs of exciting the symmetric stretching mode are significantly larger than the corresponding DCSs of exciting the asymmetric stretching mode in the backward scattering. Meanwhile, the sideways scattering in the backward hemisphere becomes dominant although the forward scattering is also nonnegligible, implying that the direct rebound mechanism becomes more and more important. Consequently, the dominance of symmetric stretching modes over asymmetric stretching

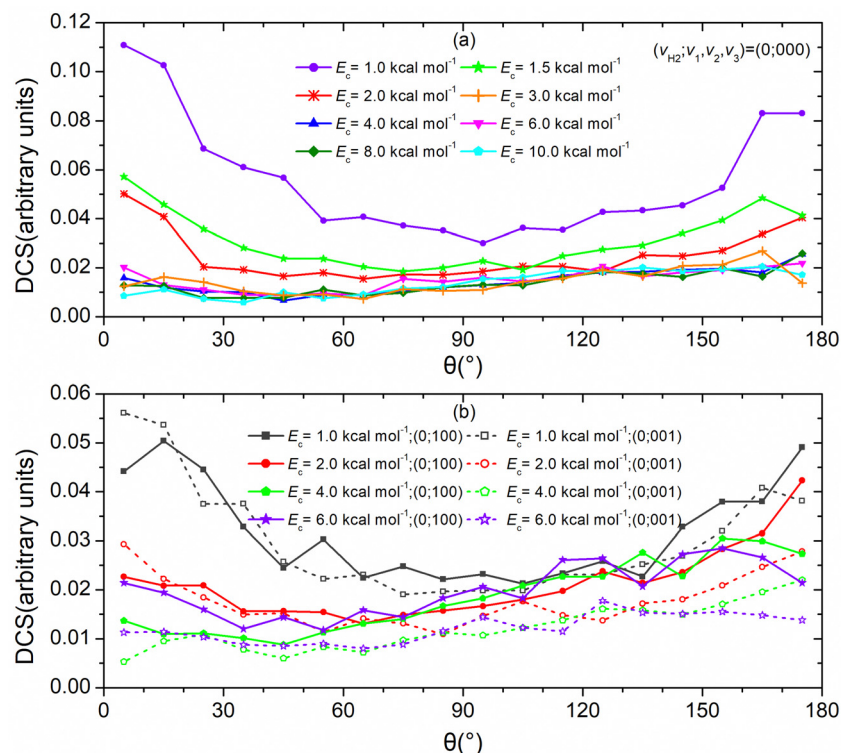


Fig. 7 (a) Differential cross sections (DCSs) of the  $\text{NH}_2^+ + \text{H}_2 \rightarrow \text{NH}_3^+ + \text{H}$  reaction from the reactant ground state with the collision energy  $E_c$  fixed at 1.0, 1.5, 2.0, 3.0, 4.0, 6.0, 8.0, and 10.0  $\text{kcal mol}^{-1}$ , respectively. (b) DCSs of the  $\text{NH}_2^+ + \text{H}_2 \rightarrow \text{NH}_3^+ + \text{H}$  reaction from the fundamental states of the symmetric and asymmetric stretching modes of  $\text{NH}_2^+$  with the collision energy taken to be 1.0, 2.0, 4.0, and 6.0  $\text{kcal mol}^{-1}$ .

modes mainly originates from the prevalence of the indirect mechanism at low collision energies and the rebound mechanism at high collision energies.

### C. Kinetics

The calculated thermal rate coefficients between 10 and 300 K are plotted in Fig. 8, together with the available experimental and theoretical results for comparison.<sup>36–40</sup> As aforementioned, Rednyk *et al.* found that the measured rate coefficient has a

negative temperature dependence between 17 and 300 K. However, the theoretical rate coefficient predicted by the QCT method on the FI-NN PES exhibits a weak positive dependence between 15 and 40 K and a negative dependence from 40 to 300 K, analogous to Mohandas's results.<sup>41</sup> The discrepancy is possibly caused by the inherent defects of the QCT method, such as the ZPE leakage and the neglect of the quantum tunneling effect. Moreover, the results from our computations are found to be somewhat close to the Langevin rate coefficient,<sup>67</sup> which means that the reaction is relatively fast and could contribute significantly to the formation of interstellar ammonia. The calculated rate coefficients at 100 K and 300 K are  $4.75 \times 10^{-10} \text{ cm}^3 \text{ molecule}^{-1} \text{ s}^{-1}$  and  $1.83 \times 10^{-10} \text{ cm}^3 \text{ molecule}^{-1} \text{ s}^{-1}$ , respectively, which agree reasonably well with the corresponding experimental results. Indeed, the calculated rate coefficients at low temperature are slightly lower than the experimental values and the deviation increases as the temperature decreases, indicating that the quantum effect is more and more significant at cold temperatures. How strong the quantum tunneling effect behaves in the title system with a submerged barrier requires rigorous quantum dynamics calculations. It is our plan to perform quantum scattering calculations on the PES at cold temperatures in the future.

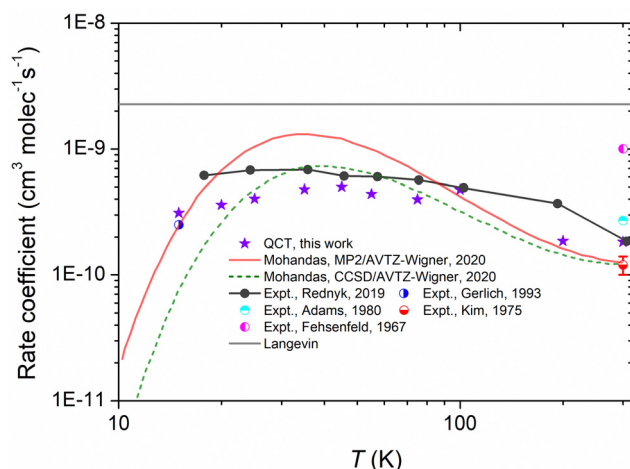


Fig. 8 Theoretical and experimental thermal rate coefficients for  $\text{NH}_2^+ + \text{H}_2 \rightarrow \text{NH}_3^+ + \text{H}$ .

## V. Conclusions

In this work, we develop an accurate full-dimensional potential energy surface for the  $\text{NH}_2^+ + \text{H}_2 \rightarrow \text{NH}_3^+ + \text{H}$  reaction fitted by



the FI-NN method with a RMSE of 0.061 kcal mol<sup>-1</sup>. A total of 65 721 energy points are sampled and calculated at the level of AE-UCCSD(T)-F12a/AVTZ. The geometry, energy and harmonic frequencies of each stationary point along the minimum energy path reproduce well the *ab initio* results.

QCT calculations are then carried out on the PES to investigate the dynamics and kinetics of the reaction. The ICS drops sharply and then becomes nearly flat with the increase of collision energy. The vibrational excitation of the reactant H<sub>2</sub> significantly enhances the reaction. Excitation of each vibrational mode of NH<sub>2</sub><sup>+</sup> has negligible effect on the reaction at high collision energies except for the symmetric stretching mode and inhibits the reaction at low collision energies. Exciting the symmetric stretching mode shows a visibly higher efficacy than exciting the asymmetric stretching mode in promoting the reaction, which is attributed to the prevalence of the indirect mechanism at low collision energies and the rebound mechanism at high collision energies. In addition, the calculated rate coefficients of the NH<sub>2</sub><sup>+</sup> + H<sub>2</sub> → NH<sub>3</sub><sup>+</sup> + H reaction exhibit a negative dependence from 40 to 300 K, in accord with the available experimental results. The Fortran subroutine of the FI-NN PES is available from the corresponding author upon reasonable request.

## Conflicts of interest

There are no conflicts to declare.

## Acknowledgements

This work is supported by the Talent Introduction Project of Hubei Polytechnic University (No. 21xjz01R to Y. Zhu) and the National Natural Science Foundation of China (No. 21973109 to H. Song).

## References

- 1 E. E. Ferguson, *Annu. Rev. Phys. Chem.*, 1975, **26**, 17–38.
- 2 W. D. Watson, *Acc. Chem. Res.*, 2002, **10**, 221–226.
- 3 D. Smith, *Chem. Rev.*, 2002, **92**, 1473–1485.
- 4 C.-Y. Ng, *J. Phys. Chem. A*, 2002, **106**, 5953–5966.
- 5 J. Mikosch, M. Weidemüller and R. Wester, *Int. Rev. Phys. Chem.*, 2010, **29**, 589–617.
- 6 A. Fridman, *Plasma Chemistry*, Cambridge University Press, Cambridge, 2012.
- 7 P. Manikandan, J. Zhang and W. L. Hase, *J. Phys. Chem. A*, 2012, **116**, 3061–3080.
- 8 Y. Wang, H. Song, I. Szabó, G. Czako, H. Guo and M. Yang, *J. Phys. Chem. Lett.*, 2016, **7**, 3322–3327.
- 9 J. Meyer and R. Wester, *Annu. Rev. Phys. Chem.*, 2017, **68**, 333–353.
- 10 T. J. Millar, C. Walsh and T. A. Field, *Chem. Rev.*, 2017, **117**, 1765–1795.
- 11 K. Song, H. Song and J. Li, *Phys. Chem. Chem. Phys.*, 2022, **24**, 10160–10167.
- 12 M. A. Dopita, D. J. Mason and W. D. Robb, *Astrophys. J.*, 1976, **207**, 102.
- 13 T. P. Snow and V. M. Bierbaum, *Annu. Rev. Anal. Chem.*, 2008, **1**, 229–259.
- 14 V. Dislaire, P. Hily-Blant, A. Faure, S. Maret, A. Bacmann and G. Pineau des Forêts, *Astron. Astrophys.*, 2012, **537**, A20.
- 15 S. S. Kumar, F. Grussie, Y. V. Suleimanov, H. Guo and H. Kreckel, *Sci. Adv.*, 2018, **4**, eaar3417.
- 16 C. E. Dateo and D. C. Clary, *J. Chem. Soc., Faraday Trans. 2*, 1989, **85**, 1685–1696.
- 17 M. González, M. Gilibert, A. Aguilar and R. Sayós, *J. Chem. Phys.*, 1993, **98**, 2927–2935.
- 18 I. Szabó, A. G. Császár and G. Czako, *Chem. Sci.*, 2013, **4**, 4362–4370.
- 19 A. Li, Y. Li, H. Guo, K. C. Lau, Y. Xu, B. Xiong, Y. C. Chang and C. Y. Ng, *J. Chem. Phys.*, 2014, **140**, 011102.
- 20 H. Song, A. Li, H. Guo, Y. Xu, B. Xiong, Y. C. Chang and C. Y. Ng, *Phys. Chem. Chem. Phys.*, 2016, **18**, 22509–22515.
- 21 H. Song, A. Li, M. Yang and H. Guo, *Phys. Chem. Chem. Phys.*, 2017, **19**, 17396–17403.
- 22 B. Olsz, I. Szabó and G. Czako, *Chem. Sci.*, 2017, **8**, 3164–3170.
- 23 Y. Zhu, L. Tian, H. Song and M. Yang, *J. Chem. Phys.*, 2019, **151**, 054311.
- 24 N. Bulut, A. Aguado, C. Sanz-Sanz and O. Roncero, *J. Phys. Chem. A*, 2019, **123**, 8766–8775.
- 25 C. M. Persson, M. De Luca, B. Mookerjee, A. O. H. Olofsson, J. H. Black, M. Gerin, E. Herbst, T. A. Bell, A. Coutens, B. Godard, J. R. Goicoechea, G. E. Hassel, P. Hily-Blant, K. M. Menten, H. S. P. Müller, J. C. Pearson and S. Yu, *Astron. Astrophys.*, 2012, **543**, 1432.
- 26 C. M. Persson, M. Hajigholi, G. E. Hassel, A. O. H. Olofsson, J. H. Black, E. Herbst, H. S. P. Müller, J. Cernicharo, E. S. Wiström, M. Olberg, Å. Hjalmarson, D. C. Lis, H. M. Cuppen, M. Gerin and K. M. Menten, *Astron. Astrophys.*, 2014, **567**, A130.
- 27 O. Lakhmanskaya, M. Simpson, S. Murauer, M. Notzold, E. Endres, V. Kokouline and R. Wester, *Phys. Rev. Lett.*, 2018, **120**, 253003.
- 28 A. C. Cheung, D. M. Rank, C. H. Townes, D. D. Thornton and W. J. Welch, *Phys. Rev. Lett.*, 1968, **21**, 1701–1705.
- 29 P. J. Benson and P. C. Myers, *Astrophys. J., Suppl. Ser.*, 1989, **71**, 89–108.
- 30 M. Tafalla and R. Bachiller, *Astrophys. J.*, 1995, **443**, L37.
- 31 T. Pillai, F. Wyrowski, S. J. Carey and K. M. Menten, *Astron. Astrophys.*, 2006, **450**, 569–583.
- 32 E. Herbst and W. Klemperer, *Astrophys. J.*, 1973, **185**, 505.
- 33 R. Le Gal, P. Hily-Blant, A. Faure, G. Pineau des Forêts, C. Rist and S. Maret, *Astron. Astrophys.*, 2014, **562**, A83.
- 34 M. Gerin, D. A. Neufeld and J. R. Goicoechea, *Annu. Rev. Astron. Astrophys.*, 2016, **54**, 181–225.
- 35 K. Acharyya and E. Herbst, *Astrophys. J.*, 2015, **812**, 142.
- 36 F. C. Fehsenfeld, A. L. Schmeltekopf and E. E. Ferguson, *J. Chem. Phys.*, 1967, **46**, 2802–2808.
- 37 J. K. Kim, *J. Chem. Phys.*, 1975, **62**, 45.
- 38 N. G. Adams, D. Smith and J. F. Paulson, *J. Chem. Phys.*, 1980, **72**, 288–297.

- 39 D. Gerlich, *J. Chem. Soc., Faraday Trans.*, 1993, **89**, 2199–2208.
- 40 S. Rednyk, Š. Roučka, A. Kovalenko, T. D. Tran, P. Dohnal, R. Plašil and J. Glosik, *Astron. Astrophys.*, 2019, **625**, A74.
- 41 S. Mohandas, R. O. Ramabhadran and S. S. Kumar, *J. Phys. Chem. A*, 2020, **124**, 8373–8382.
- 42 H. Han, H. Song, J. Li and H. Guo, *J. Phys. Chem. A*, 2015, **119**, 3400–3406.
- 43 T. B. Adler, G. Knizia and H. J. Werner, *J. Chem. Phys.*, 2007, **127**, 221106.
- 44 G. Knizia, T. B. Adler and H. J. Werner, *J. Chem. Phys.*, 2009, **130**, 054104.
- 45 K. Shao, J. Chen, Z. Zhao and D. H. Zhang, *J. Chem. Phys.*, 2016, **145**, 071101.
- 46 R. Chen, K. Shao, B. Fu and D. H. Zhang, *J. Chem. Phys.*, 2020, **152**, 204307.
- 47 L. Tian, Y. Zhu, H. Song and M. Yang, *Phys. Chem. Chem. Phys.*, 2019, **21**, 11385–11394.
- 48 Y. Zhu, L. Ping, M. Bai, Y. Liu, H. Song, J. Li and M. Yang, *Phys. Chem. Chem. Phys.*, 2018, **20**, 12543–12556.
- 49 L. Ping, Y. Zhu, A. Li, H. Song, Y. Li and M. Yang, *Phys. Chem. Chem. Phys.*, 2018, **20**, 26315–26324.
- 50 M. Pan, H. Xiang, Y. Li and H. Song, *Phys. Chem. Chem. Phys.*, 2021, **23**, 17848–17855.
- 51 T. J. Lee, *Chem. Phys. Lett.*, 2003, **372**, 362–367.
- 52 B. Ruscic and D. H. Bross, Active Thermochemical Tables (ATcT) values based on ver. 1.122r of the Thermochemical Network, 2021, available at ATcT.anl.gov, 2021.
- 53 H.-J. Werner, P. J. Knowles, G. Knizia, F. R. Manby, M. Schütz and others, *MOLPRO, version 2012.1, a package of ab initio programs*, 2012, see <https://www.molpro.net>.
- 54 M. J. Frisch, G. W. Trucks, H. B. Schlegel, G. E. Scuseria, M. A. Robb, J. R. Cheeseman, G. Scalmani, V. Barone, G. A. Petersson, H. Nakatsuji, X. M. Li and others, *Gaussian 09, Revision B.01*, Gaussian, Inc., Wallingford CT, 2009.
- 55 M. A. Collins, *Theor. Chem. Acc.*, 2002, **108**, 313–324.
- 56 J. Li, B. Jiang and H. Guo, *J. Chem. Phys.*, 2013, **139**, 204103.
- 57 B. Jiang and H. Guo, *J. Chem. Phys.*, 2013, **139**, 054112.
- 58 L. M. Raff, R. Komanduri, M. Hagan and S. T. S. Bukkapatnam, *Neural Networks in Chemical Reaction Dynamics*, Oxford University Press, Oxford, 2012.
- 59 Z. Xie and J. M. Bowman, *J. Chem. Theory Comput.*, 2010, **6**, 26–34.
- 60 M. T. Hagan and M. B. Menhaj, *IEEE Trans. Neural Netw.*, 1994, **5**, 989–993.
- 61 Z.-H. Zhou, J. Wu and W. Tang, *Artif. Intell.*, 2002, **137**, 239–263.
- 62 W. L. Hase, R. J. Duchovic, X. Hu, A. Komornicki, K. F. Lim, D. H. Lu, G. H. Peslherbe, K. N. Swamy, S. V. Linde and A. Varandas, *VENUS96: A General Chemical Dynamics Computer Program*, QCPE Bulletin, 1996.
- 63 Y. Zhu, L. Tian, H. Song and M. Yang, *J. Phys. Chem. A*, 2020, **124**, 6794–6800.
- 64 J. L. B. J. Zheng, R. Meana-Pañeda, S. Zhang, B. J. Lynch, J. C. Corchado, Y.-Y. Chuang, P. L. Fast, W.-P. Hu, Y.-P. Liu, G. C. Lynch, K. A. Nguyen, C. F. Jackels, A. F. Ramos, B. A. Ellingson, V. S. Melissas, J. Villa, I. Rossi, E. L. Coitino, J. Pu and T. V. Albu, *POLYRATE, version 9.7*, Department of Chemistry and Supercomputing Institute, University of Minnesota, 2007.
- 65 H. Xiang, Y. Lu, H. Song and M. Yang, *Chin. J. Chem. Phys.*, 2022, **35**, 200–206.
- 66 X. Lu, B. Fu and D. H. Zhang, *Phys. Chem. Chem. Phys.*, 2020, **22**, 26330–26339.
- 67 G. Gioumousis and D. P. Stevenson, *J. Chem. Phys.*, 1958, **29**, 294–299.